Simulation model of Reactive Nitrogen species in an urban atmosphere using a Deep neural network: RNDv1.0

Junsu Gil[1], Meehye Lee[1], Jeonghwan Kim[2], Gangwoong Lee[2], Joonyoung Ahn[3], Cheol-Hee Kim[4]

[1] Department of Earth and Environmental Sciences, Korea University, Seoul, South Korea
[2] Department of Environmental Science, Hankuk University of Foreign Studies, Yongin, South Korea
[3] Air Quality Forecasting Center, Climate and Air Quality Research Department, National Institute of Environmental Research (NIER), Incheon, South Korea
[4] Department of Atmospheric Sciences, Pusan National University, Busan, South Korea

Correspondence to: Meehye Lee (meehye@korea.ac.kr)

Abstract. Nitrous acid (HONO) plays an important role in the formation of ozone and fine aerosols in the urban atmosphere. In this study, a new simulation approach is presented to calculate the HONO mixing ratios using a deep neural technique based on measured variables. The "Reactive Nitrogen species simulation using deep neural network (RND)" is implemented in Python. The first version of RND (RNDv1.0) is trained, validated, and tested with HONO measurement data obtained in Seoul from 2016 to 2021. RNDv1.0 is constructed using k-fold cross validation and evaluated with index of agreement, correlation coefficient, root mean squared error, and mean absolute error. The results show that RNDv1.0 adequately represents the main characteristics of the measured HONO, and it is thus proposed as a supplementary model for calculating the HONO mixing ratio in a polluted urban environment.

1. Introduction

Surface ozone (O_3) pollution has worsened over continental areas (Arnell et al., 2019;Monks et al., 2015;Varotsos et al., 2013;IPCC, 2014). Particularly, a warmer climate is expected to increase the surface O_3 concentrations and peak levels in polluted regions depending on its precursor levels (IPCC, 2021). As a short-lived climate pollutant (SLCP), O_3 interacts with the global temperature via positive feedback (Shindell et al., 2013;Myhre et al., 2017;Stevenson et al., 2013). Therefore, accurate predictions of the mixing ratios and variations of the surface O_3 are essential. While operational models such as the community multiscale air

quality (CMAQ) have been widely used for this purpose, uncertainties still arise from poorly understood chemical mechanisms involving reactive nitrogen oxides (NO_y) and volatile organic compounds (VOCs), and the lack of their measurements (Mallet and Sportisse, 2006;Canty et al., 2015;Akimoto et al., 2019;Shareef et al., 2019;Cheng et al., 2022).

In the urban atmosphere, NO_y typically includes NO_x (NO + NO_2), HONO, HNO_3, organic nitrates (e.g., PAN), NO_3, N_2O_3, and particulate NO_3^-. These species are produced and recycled through photochemical reactions until they are removed through wet or dry deposition (Liebmann et al., 2018;Brown et al., 2017;Wang et al., 2020;Li et al., 2020). NO_y plays an important role in critical environmental issues concerning the Earth's atmosphere from local air pollution to global climate change (Sun et al., 2011;Ge et al., 2019). The oxidation of NO to NO_2 and finally to HNO_3 is the backbone of the chemical mechanism producing ozone (O_3) and $PM_{2.5}$ (particulate matter with size $\leq$ 2.5 μm), and determines the oxidization capacity of the atmosphere. Recently, as O_3 has still increased even with decreasing NO_x emissions over many regions, including East Asia, interest in the heterogeneous reaction of NO_y, which is yet to be understood, has increased (Brown et al., 2017;Stadtler et al., 2018). Currently, the lack of measurement of individual NO_y species is hindering a comprehensive understanding of the heterogeneous reactions (Anderson et al., 2014;Wang et al., 2017b;Chen et al., 2018b;Akimoto and Tanimoto, 2021;Stadtler et al., 2018).

In particular, the evidence for the heterogeneous formation of HONO in relation to high $PM_{2.5}$ and O_3 occurrences in urban areas is increasing (e.g., (Li et al., 2021b)). As an OH reservoir, HONO expedites the photochemical reactions involving VOCs and NO_x in the early morning, leading to O_3 and fine aerosol formation. Nonetheless, its formation mechanism has not been elucidated sufficiently enough to be constrained in conventional photochemical models. In addition to the reaction of NO with OH (Bloss et al., 2021), various pathways of HONO formation have been suggested via laboratory experiments, field measurements, and model simulations: direct emissions from vehicles (Li et al., 2021a) and soil (Bao et al., 2022), photolysis of particulate nitrate (Gen et al., 2022), and heterogeneous conversion of NO_2 on various aerosol surfaces (Jia et al., 2020), ground surface (Meng et al., 2022), and microlayers of the sea surface (Gu et al., 2022). Among these, the heterogeneous reaction mechanism on the surface is of major interest.

HONO has been mostly measured during intensive campaigns in urban areas using various techniques, such as a long path absorption photometer (Kleffmann et al., 2006;Xue et al., 2019), chemical ionization mass spectrometry (Levy et al., 2014;Roberts et al., 2010), ion chromatography (VandenBoer et al., 2014;Gil et al., 2020;Ye et al., 2016;Xu et al., 2019), monitor for aerosols and gases in ambient air (MARGA) (Xu et al., 2019), and quantum cascade - tunable infrared laser differential absorption spectrometry (QC-TILDAS) (Lee et al., 2011;Gil et al., 2021). Among these methods, QC-TILDAS has served as a reference for the intercomparison of measurement data obtained using different techniques due to its high time resolution and stability (Pinto et al., 2014). Previous studies have reported that the maximum HONO of several ppb levels has been observed at nighttime. In comparison, the WRF-Chem and RACM2 model captured approximately 67 %–90 % of the observed HONO in megacities such as Beijing (Tie et al., 2013;Liu et al., 2019).

In recent years, machine learning (ML) methods have been employed in the atmospheric science field for pattern classification (e.g., new particle formation event) and forecasting and spatiotemporal modeling of O_3 and $PM_{2.5}$ (Arcomano et al., 2021;Shahriar et al., 2020;Krishnamurthy et al., 2021;Cui and Wang, 2021;Joutsensaari et al., 2018;Chen et al., 2018a;Kang et al., 2021). Among the ML methods, the neural network (NN) architecture is widely used owing to its powerful ability to process large volumes of data. In particular, a multilayer artificial NN (ANN), referred to as a deep NN (DNN), employes statistical methods to learn nonlinear relationships within the data and yield optimal solutions for a target species without prior knowledge of the underlying physicochemical processes (Reichstein et al., 2019;Schultz et al., 2021). DNN is more beneficial than other NN architecture, such as convolution NN or long-short term memory, because it works well for discrete spatiotemporal data. Generally, the performance of DNN is similar to or better than that of other ML methods for small as well as large datasets (Baek and Jung, 2021;Dang et al., 2021;Sumathi and Pugalendhi, 2021).

The DNN method requires lots of data to employ it as atmospheric chemical constituent estimation; therefore, the size of the measurement data is a limiting factor for trace species, such as HONO, that are not routinely measured. In this regard, previous studies had been attempted to estimate the daily average HONO mixing ratio by employing ensemble ML models with satellite measurements (Cui and Wang, 2021). Furthermore, a simple NN architecture

3

95   using ground measurement variables that is believed to be deeply involved in HONO formation,

96   was used to calculate the hourly HONO mixing ratio (Gil et al., 2021). The accuracy of the

97   hourly HONO estimated from input variables, such as aerosol surface areas and mixed layer

98   height, is rated better than the daily HONO estimate.

99   This study aims to develop a user-friendly "reactive nitrogen species simulation using

100   DNN' model (RNDv1.0) that estimates the HONO mixing ratios from the real-time

101   measurements of criteria pollutants and meteorological variables. This study is the first to

102   calculate the HONO mixing ratios using RNDv1.0. The entire construction process is

103   comprehensively described, and the performance is evaluated via comparison with the results

104   of simulations using a commonly used model and observations over several years.

105

2. Model description

107

108   The RNDv1.0 development follows systematic steps that are similar to a general ML

109   model construction workflow, including data collection, preprocessing data, building the DNN,

110   training, and validating the model, and testing the model performance (Figure 1). RNDv1.0 is

111   written in Python, and the libraries necessary to build and operate RNDv1.0 are listed in Table

112   1. The dataset used to train, test, and validate can be downloaded from Gil (2021).

113

2.1. Collection of measurement data for model construction

115

116   To construct RNDv1.0, measurement data were obtained, including HONO, reactive

117   gases, and meteorological variables. Note that the HONO measurement data were used for

118   model construction but not required to run the RND model. The HONO mixing ratio was

119   measured in Seoul using a QC-TILDAS system during May–June 2016, June 2018, and April–

120   June 2019 (Lee et al., 2011;Gil et al., 2021), and a MARGA system during May–June 2021 and

121   October–November 2021 (Gil, 2022). When testing and evaluating the atmospheric HONO

122   measurement methods, QC-TILDAS was chosen as the reference method to compare the

123   ambient HONO mixing ratios measured using several different techniques owing to its

124 advantages of low detection limits (~0.1 ppbv) and high temporal resolution (Pinto et al., 2014).

125 More details on measurements can be found elsewhere (Gil et al., 2021;Gil, 2022).

126 HONO was measured at the Olympic Park (37.52° N, 127.12° E) during the Korea–

127 United States Air Quality (KORUS-AQ) study in 2016 (Kim et al., 2020;Gil et al., 2021), at the

128 campus of Korea University (37.59° N, 127.03° E) in 2018 and 2021, and at the site near the

129 Korea University campus (37.59° N, 127.08° E) in 2019 (NIER, 2020) (Figure S1). In addition

130 to HONO, trace gases including O_3, NO_2, CO, and SO_2 as well as meteorological variables

131 including temperature (T), relative humidity (RH), wind speed (WS), and wind direction (WD)

132 were measured. Note that HONO was not significantly correlated with any of these variables

133 (Figure S2). The measurement statistics for the entire experimental periods are presented in

134 Table 2 and Table S1. In brief, the 10th and 90th percentile mixing ratios of hourly HONO, NO_2,

135 and O_3, were 0.3 and 2.0 ppbv, 10.0 and 47.0 ppbv, and 8.0 and 75.0 ppbv, respectively.

136

137 **2.2. Data preprocessing**

138

139 The observation dataset was prepared for RNDv1.0 model construction. As input

140 variables, hourly measurements of chemical and meteorological variables were used, including

141 the mixing ratios of O_3, NO_2, CO, and SO_2, along with T, RH, WS, WD, and solar zenith angle

142 (SZA) to estimate the target species, HONO, as the output. The WD in degrees was converted

143 to a cosine value for continuity. In the last step of data processing, hourly measurement sets

144 were removed from the input data set if any of the nine variables were missing. Finally, 54.2 %

145 of all the available measurement data (2847 data points) were used to construct and evaluate

146 RNDv1.0.

147 Since the measurements of the considered nine variables varied over a wide range in

148 different units, they were normalized to avoid bias during the calculations. Among the widely

149 used normalization methods, *min–max scaling* method was adopted, and the input variables

150 were normalized against the minimum and maximum values herein (Eq. 1):

151

152 $$x_{sca} = \frac{x_{raw} - F_2(X)}{F_1(X)},$$ (Eq. 1)

153

154   where x_{raw} is the raw data, x_{sca} is the scaled value, and the scale factors of F_1 and F_2 correspond

155   to the maximum-minimum and minimum values of the input variable (X), respectively, which

156   are listed in Table 2.

157

158   **2.3. Neural network architecture and hyperparameters**

159

160   The network was built using the above input variables to calculate HONO. RNDv1.0

161   comprises five hidden layers (Figure 2), which employ an exponential linear unit (ELU) as an

162   activation function (Eq. 2).

163

164    $$\text{ELU}: \phi(x) = \begin{cases} e^x - 1 \ (x < 0) \\ x \ (x \geq 0) \end{cases}. \qquad \text{(Eq. 2)}$$

165

166   In a DNN, an activation function creates a nonlinear relationship between an input

167   variable and an output variable. When constructing a DNN model, ELU affords the advantage

168   of a fast training process and exhibits better performance in handling negative values than other

169   activation functions (Wang et al., 2017a;Ding et al., 2018). Moreover, the mean squared error

170   and Adam optimizer were applied as the loss function and optimization function, respectively.

171   The learning rate, epoch, and batch were set as 0.01, 100, and 32, respectively.

172

173   **2.4. Model training and k-fold cross validation**

174

175   RNDv1.0 was trained, validated, and tested with the HONO measurements obtained

176   during May–June 2016 and June 2018, April–June 2019, and May–June 2021 and October–

177   November 2021, respectively (Figure 3). The number of data used for the training and

178   validation was 1122 and that for testing was 1725.

179   Using the hyperparameters specified in the previous section, the model performance

180   was first validated using the k-fold cross validation (KFCV) method, which is especially useful

181   for small datasets (Bengio and Grandvalet, 2003). In the KFCV method (Figure 3), the entire

182   data are randomly divided into k subsets, of which k − 1 sets are used for training and the

183   remaining one is used for validation. In this study, k was set to 5. The accuracy was determined

184   via index of agreement (IOA), which is expressed as follows (Eq. 3):

185

186    $$IOA = 1 - \frac{\sum_{i=1}^{n}(O_i - P_i)^2}{\sum_{i=1}^{n}(|P_i - \bar{O}| + |O_i - \bar{O}|)^2},$$ (Eq. 3)

187

188   where O_i, P_i, $\bar{O}$, and n are the observed value, predicted value, average of the observed values,

189   and number of nodes, respectively.

190   As IOA varies according to the number of nodes, it was calculated for the measured

191   ($HONO_{obs}$) and calculated ($HONO_{mod}$) mixing ratios by varying the number of nodes from 0 to

192   100 in each hidden layer. The best performance was obtained with 41 nodes, for which the

193   average IOA was 0.89 ± 0.01 (Figure 4). The high IOA value signifies that the performance of

194   RNDv1.0 is adequate, and it is capable of simulating the ambient HONO mixing ratio using the

195   routinely measured criteria pollutants and meteorological variables.

196   The performance of RNDv1.0 was compared with that of other models, including

197   CMAQv5.3.1 (Appel et al., 2021), random forest (RF), and single-layer ANN (Gil et al., 2021),

198   using the 2016 measurement data. The RF model was constructed using the KFCV method and

199   the same input variables as RNDv1.0 (Figure S4). Its performance was evaluated based on mean

200   absolute error (MAE), root mean square deviation (RMSE), and Pearson correlation coefficient

201   (r):

202

203    $$MAE = \frac{\sum_{i=1}^{n}|O_i - P_i|}{n},$$ (Eq. 4)

204    $$RMSE = \sqrt[2]{\frac{\sum_{i=1}^{n}(O_i - P_i)^2}{n}},$$ (Eq. 5)

205    $$r = \frac{cov(O,P)}{\sigma_O \sigma_P},$$ (Eq. 6)

207 where σ and *cov* denote the standard deviation and covariance, respectively.

208   All models except CMAQ simulated the measured HONO mixing ratio fairly well

209 (Figure 5). CMAQ not only underestimated the measured HONO but also failed to represent its

210 diurnal variation (Figure 6). The statistical information about the performance of the four

211 models is presented in Table 3. The mean HONO mixing ratio measured and calculated using

212 CMAQ, RF, ANN, and RNDv1.0 was 0.94, 0.09, 0.95, 0.88, and 0.89 ppbv, respectively. Of the

213 four models, RF exhibited the best performance followed by RND. ANN advantageously

214 calculates HONO more accurately than RND as it uses more input variables, but it has a lower

215 data capture rate (41.5 %) compared to RND (97.7 %) or RF (85.3 %).

216

2.5. Model test

218

219   RNDv1.0 and the RF model were tested using data obtained in June 2018, April 2019,

220 and May–June 2021 and October–November in 2021, which were not used for RNDv1.0

221 training (Figure 3). Note that the RF model outperformed the other three models in the training

222 and validation process (Figure 5). Although the performance of RNDv1.0 was slightly lower

223 than that of the RF model, simulated and measured HONO mixing ratios were in good

224 agreement. Interestingly, the performance of the RF model was much worse than RNDv1.0 in

225 the testing process (Figure 7). The IOA and correlation coefficient of the RF model were

226 extremely low (0.29 and −0.02, respectively).

227   The performance of RNDv1.0 was slightly lower than that of the RF model, but it well

228 traced the HONO mixing ratio. Among the test dataset, the early winter (October–November)

229 data are particularly valuable for demonstrating the applicability of RNDv1.0 because they stem

230 from different weather conditions than the training dataset. For example, HONO mixing ratios

231 reached over 4 ppbv when the daily average $PM_{2.5}$ concentration increased to $120\ \mu g\ m^{-3}$ during

232 severe haze pollution events. Therefore, in the next step, the performance of RNDv1.0 was

233 compared for the two cases by dividing the testing dataset into a group in which all input

234 variables fall within the range of the training dataset and a group which does not meet this

criterion. In RNDv1.0, there was no significant difference in performance between the two groups (Figure S5 and Table S2). When the data in which at least one input variable does not fall within the range of the training dataset were excluded from the test dataset, no significant difference was observed in the performance of RNDv1.0 between the two that meet same atmospheric conditions or do not meet the criteria (Figure S5 and Table S2). These extreme atmospheric conditions can make the model performance be worsened. Except for these extremes, RNDv1.0 well traced the variation of the HONO mixing ratio. These results demonstrate the applicability of RNDv1.0, which is not strictly constrained by atmospheric conditions. The influence of input variable are further analyzed in the next section.

2.6. Bootstrap test and feature importance

A simple bootstrapping test was conducted for both RNDv1.0 and the RF model to evaluate the relative importance of the input variable to the HONO estimates. In this analysis, each variable was set to zero and MAE was calculated as an evaluation metrics (Kleinert et al., 2021). Among the nine input variables of RNDv1.0, NO_2 was found to have the greatest influence on HONO concentration, followed by RH and T (Table 5). The highest MAE of 0.59 ppbv could be considered as the maximum uncertainty of RNDv1.0 due to the input variable. The bootstrap test result well agreed with that of our previous study (Gil et al., 2021), where more variables such as aerosol surface area and mixing layer height were incorporated into the model, it highlights the crucial role of precursor gases and heterogeneous conversion in HONO formation.

In contrast, in the RF model, O_3 was the most important variable. This is likely due to the distinct inverse relationship between O_3 and HONO in the diurnal patterns, and the O_3 variations over a wide range. In conjunction with the evaluation of the test dataset presented in the previous section, the results of the feature importance for the two models demonstrate the ability of RNDv1.0 to simulate the HONO mixing ratio more adequately in urban areas compared to the RF model. Thus, it is reasonable to state that RNDv1.0 constructed using routinely measured criteria pollutants and meteorological variables can sufficiently capture the HONO variability in the urban atmosphere.

9

265

3. Operation and application of RNDv1.0

267

268   The RNDv1.0 package is provided as an operational model, and the .h5 files that can
269   be opened in Python. To run RNDv1.0, the measurement data for nine input variables are
270   required and needed to be properly prepared, as described in Section 2.2. Once the input data
271   are ready, open RNDv1.0 with the input data files using the code provided in the example
272   (Figure S3). Then, RNDv1.0 calculates and presents the HONO results as scaled values (x_{sca}),
273   which then can be converted to the HONO mixing ratio (ppbv) via the two scale factors shown
274   in Table 2 (Eq. 5):

275

276    $$HONO \ (ppbv) = HONO_{sca} \times F_1(HONO) + F_2(HONO). \tag{5}$$

277

278   The HONO calculated using Eq. 5 can be applied to an urban photochemical cycle
279   simulation. As is already known, the photolysis of HONO is a major source of OH radicals in
280   the early morning when the OH level is low, and this OH affects daytime O_3 formation through
281   photochemical reactions with VOCs and NO_x, which are primarily emitted during the morning
282   rush hour in urban areas. Furthermore, the OH produced from HONO promotes the
283   photochemical oxidation of SO_2 and VOCs, leading to aerosol formation. However, the HONO
284   formation mechanism is still poorly understood, which hinders the accurate simulation of O_3
285   and fine aerosols as well as HONO in conventional photochemical models.

286   The framework for 0-dimension atmospheric modeling (F0AM), which utilizes the
287   MCM v3.3.1 chemical reaction mechanisms (Wolfe et al., 2016), can be used to simulate the
288   diurnal variation of O_3 with the measurements of several reactive gases (NO, NO_2, CO, HCHO,
289   VOCs, and HONO). Detailed information about F0AM can be found in
290   (https://sites.google.com/site/wolfegm/models) and in previous studies (Wolfe et al., 2016; Gil
291   et al., 2020). When the F0AM model is run without HONO, it is unable to reproduce the
292   concentration and diurnal cycle of the observed O_3 (Figure 8). In comparison, the model well
293   simulates the O_3 within 2 ppbv when HONO is considered, which is the result of RND v1.0.

294 This is mainly due to the missing OH produced by HONO photolysis in the early morning. Its

295 production rate is estimated to be 0.57 pptv s^{-1}, contributing approximately 2.28 pptv to the OH

296 budget during 06:00–11:00 (Local Sun Time) (Gil et al., 2021). Given that OH is mainly

297 produced from the photolysis of O_3 under high sun, the early morning supply of OH from

298 HONO photolysis will expedite the photochemical cycle involving NO_x and VOCs, promoting

299 O_3 and secondary aerosol formation. The presence of HONO in the photochemical model

300 allows for the accurate estimation of OH radicals; thus, the incorporation of RNDv1.0 into

301 conventional models will improve their overall performance.

302

303 **4. Summary and implications**

304

305   In this study, we developed the RND model to calculate the mixing ratio of NO_y in

306 urban atmosphere using a DNN along with measurement data. The target species of RNDv1.0

307 is HONO, and its mixing ratio is calculated using criteria pollutants, including O_3, NO_2, CO,

308 and SO_2, as well as meteorological variables, including T, RH, WS, WD, and SZA. These

309 variables are routinely measured through monitoring networks. RNDv1.0 was trained and

310 validated using the HONO measurements data obtained in Seoul by adopting a KFCV method

311 and tested with other HONO datasets. The test results demonstrate that RNDv1.0 adequately

312 captures the characteristic variation of HONO.

313   RNDv1.0 was constructed using the measurements made in a high NO_x environment where

314 the maximum NO_2 reached about 80 ppbv. During the measurement period, the HONO mixing

315 ratio was increased up to about 7 ppb under the influence of air masses originating from China.

316 When applying RNDv1.0 to regions or times heavily affected by transport, the model could

317 possibly underestimate the HONO level without more detailed information, such as

318 nanoparticles. Indeed, a previous study showed that HONO formation is closely related to the

319 surface area of particles with diameters in the range of hundreds of nanometers (Gil et al., 2021).

320 Nevertheless, RNDv1.0 is advantageously a relatively inexpensive test for measurement quality

321 control and location selection, and it supports the data used for traditional chemistry models

322 based on the current knowledge of the urban photochemical cycle. Therefore, RNDv1.0 can

323 serve as a supplementary tool for conventional forecasting models. Attempts are currently being

324 made to estimate ground HONO from satellite observations (Clarisse et al., 2011;Theys et al.,
325 2020;Armante et al., 2021), and RNDv1.0 will be useful for validating the satellite-derived
326 HONO.

327

328 **5. Acknowledgements**

329

333

334 **6. Code availability**

335

336 The RND model codes (.h5 files) with preprocessed sample data can be downloaded from
337 (Gil, 2021).

338

339 **7. Author contributions**

340

341 JG and ML designed the manuscript and developed the model code. JK, GL, and JA
342 provided the HONO measurements and CK provided the CMAQ model data. All the authors
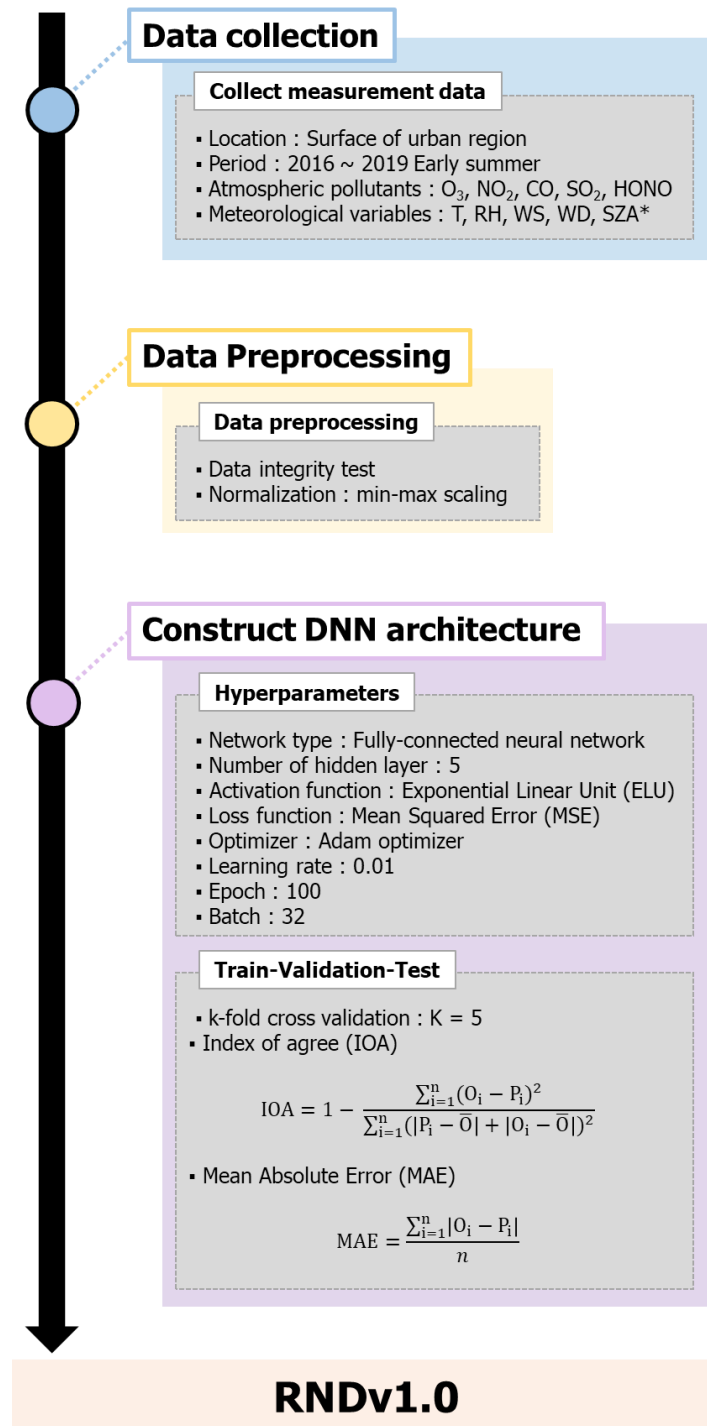343 contributed to the manuscript.

344

345 **8. Competing interests**

346

347 The authors declare that they have no conflict of interest.

348

Figures and Tables

Data collection

Collect measurement data

- Location : Surface of urban region
- Period : 2016 ~ 2019 Early summer
- Atmospheric pollutants : O_3, NO_2, CO, SO_2, HONO
- Meteorological variables : T, RH, WS, WD, SZA*

Data Preprocessing

Data preprocessing

- Data integrity test
- Normalization : min-max scaling

Construct DNN architecture

Hyperparameters

- Network type : Fully-connected neural network
- Number of hidden layer : 5
- Activation function : Exponential Linear Unit (ELU)
- Loss function : Mean Squared Error (MSE)
- Optimizer : Adam optimizer
- Learning rate : 0.01
- Epoch : 100
- Batch : 32

Train-Validation-Test

- k-fold cross validation : K = 5
- Index of agree (IOA)

$$IOA = 1 - \frac{\sum_{i=1}^{n}(O_i - P_i)^2}{\sum_{i=1}^{n}(|P_i - \overline{O}| + |O_i - \overline{O}|)^2}$$

- Mean Absolute Error (MAE)

$$MAE = \frac{\sum_{i=1}^{n}|O_i - P_i|}{n}$$

RNDv1.0

351

Figure 1. The main processes for configuring RNDv1.0 (*: calculated values)
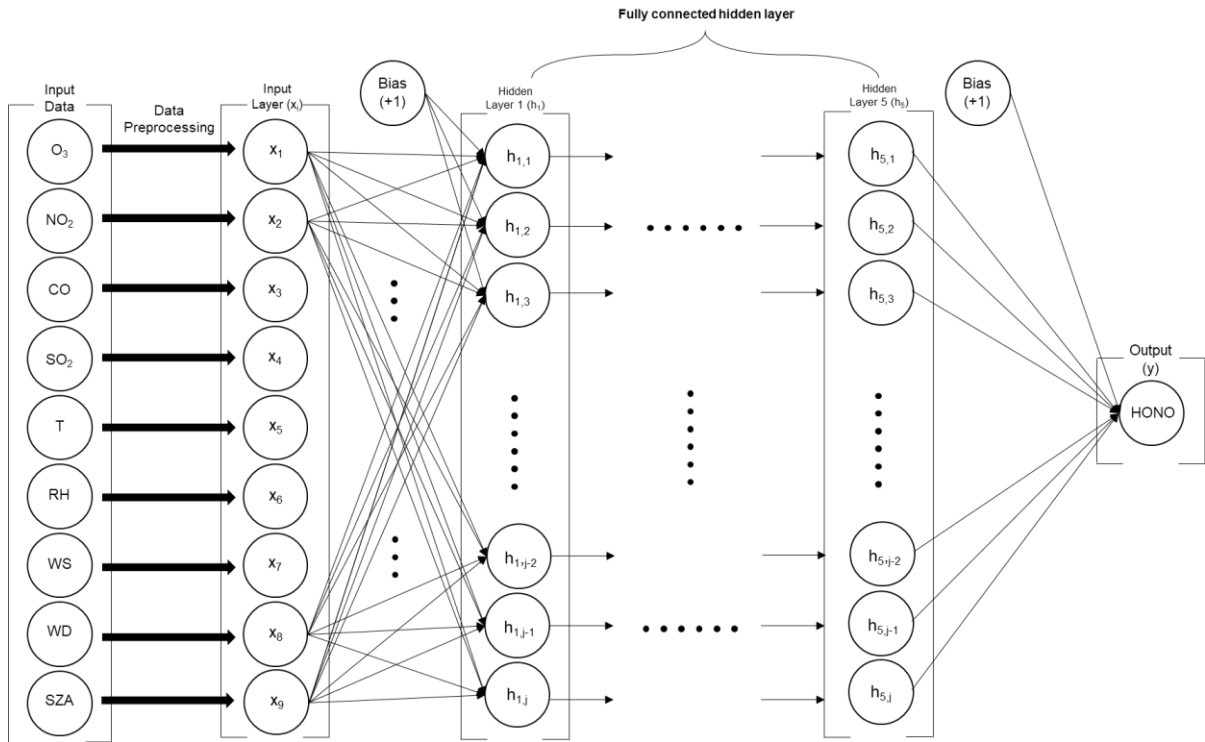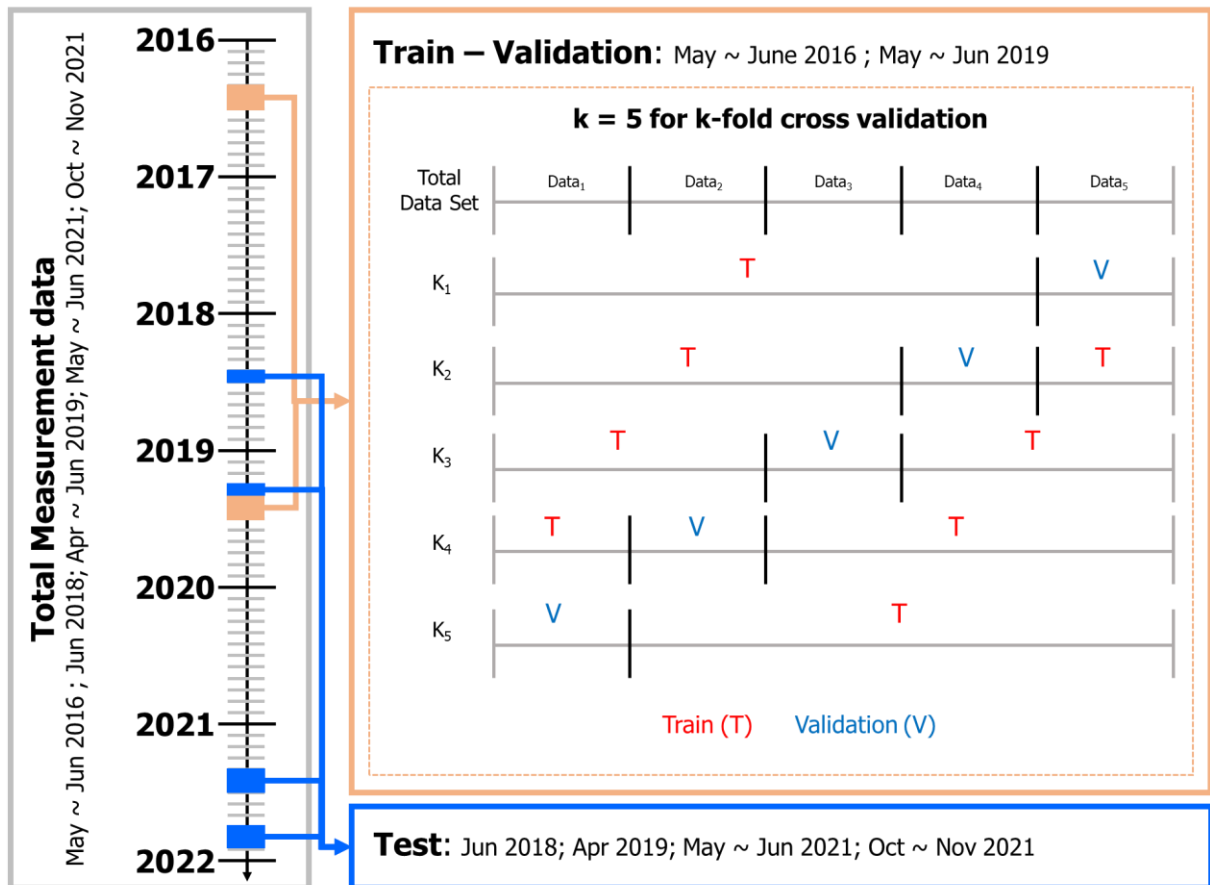
353
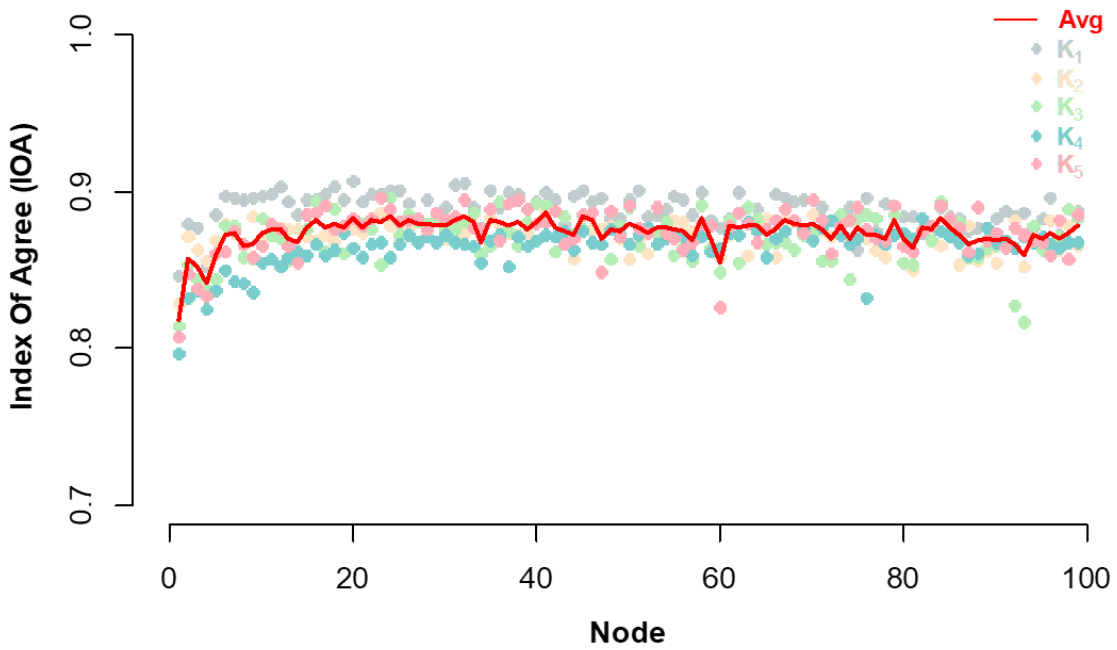354 **Figure 2.** Structure of the deep neural network built for RND v1.0.

355

356

**Figure 3.** Training, validation, and test design to build RNDv1.0 using the measurement data. The k-fold cross validation was performed using randomly divided five subsets of the training data set.

Figure 4. Index of Agreement (IOA) for k-fold cross validation. Solid circle and red line represent IOA for each validation (k = 5) and the average of five validation sets at each node number.
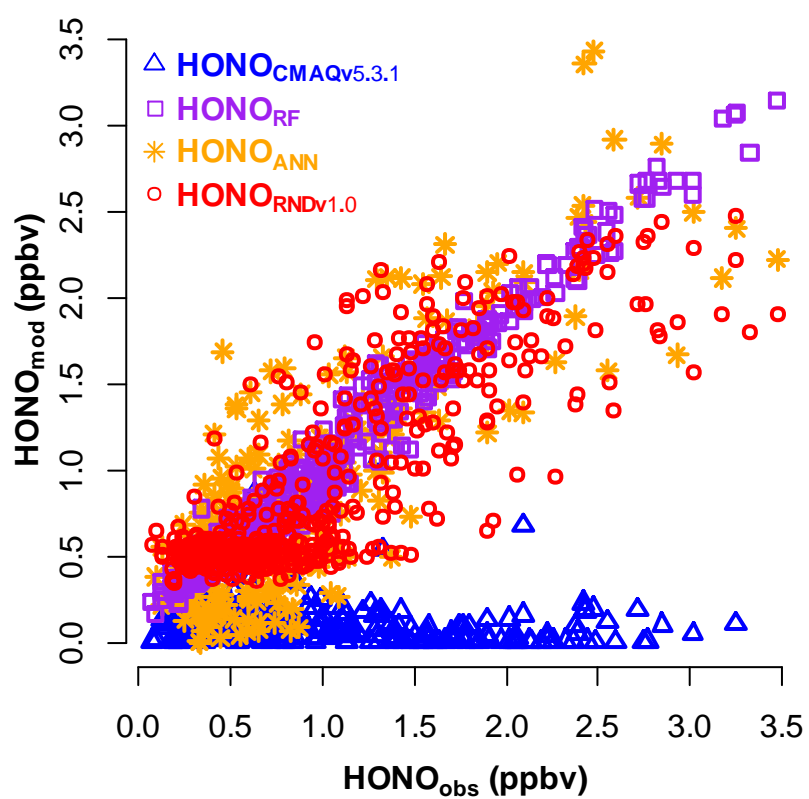
Figure 5. Comparison between the measured HONO (HONO$_{obs}$) and calculated HONO (HONO$_{mod}$) using CMAQv5.3.1 (blue triangle), RF (purple square), ANN (orange star), and RNDv1.0 (red circle) during the KORUS-AQ campaign (May–June 2016).
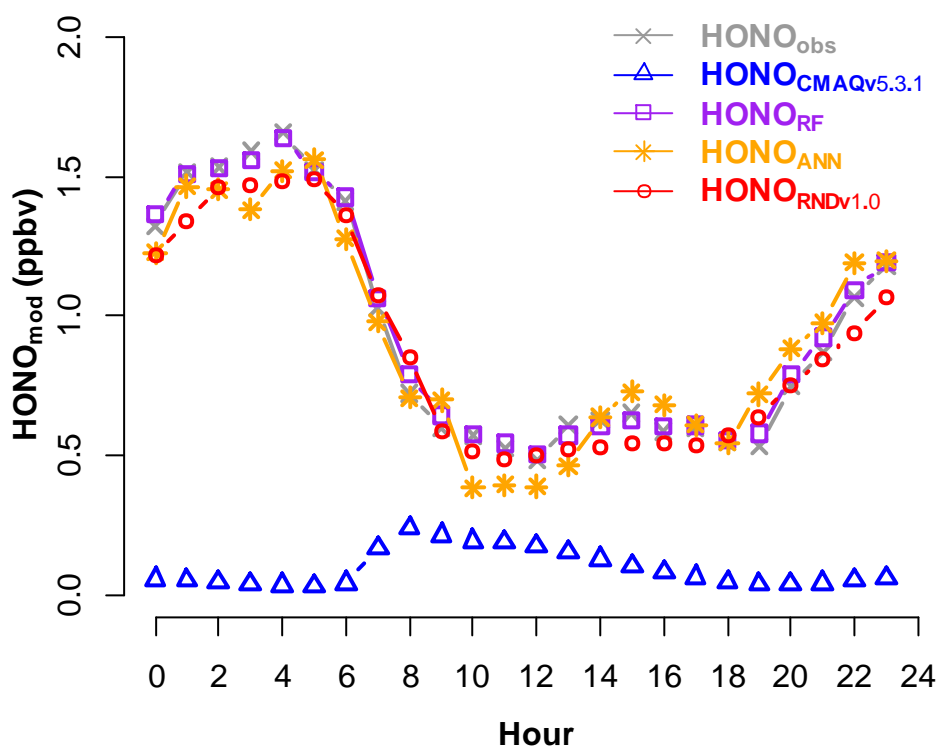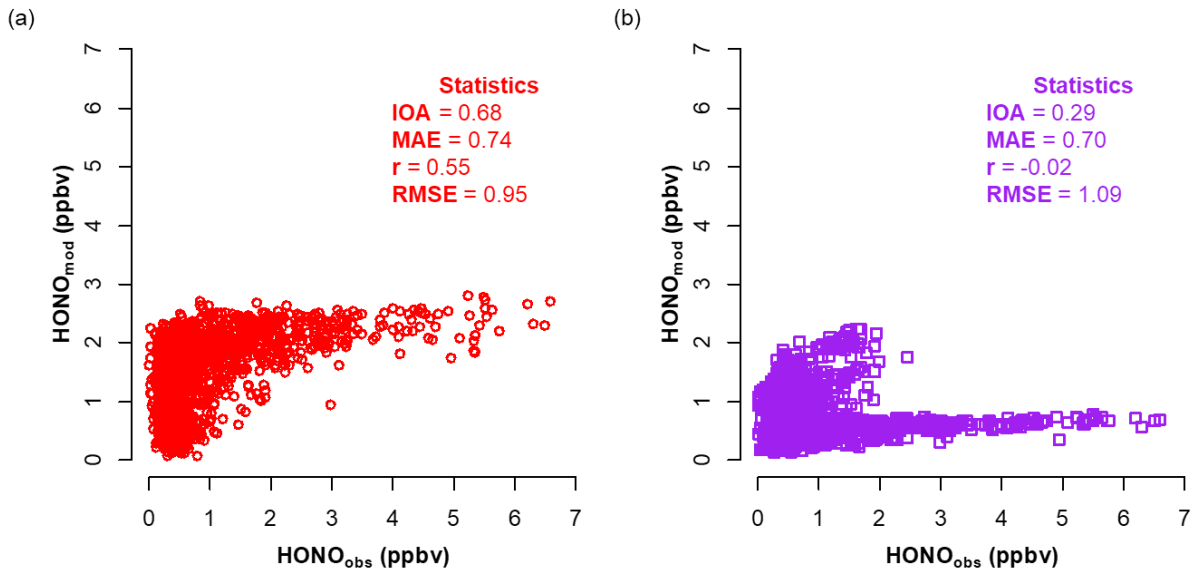
Figure 6. Average diurnal variation of the measured HONO (HONO$_{obs}$) and calculated HONO (HONO$_{mod}$) using CMAQv5.3.1 (blue triangle), RF (purple square), ANN (orange star), and RNDv1.0 (red circle) during the KORUS-AQ campaign (May–June 2016).
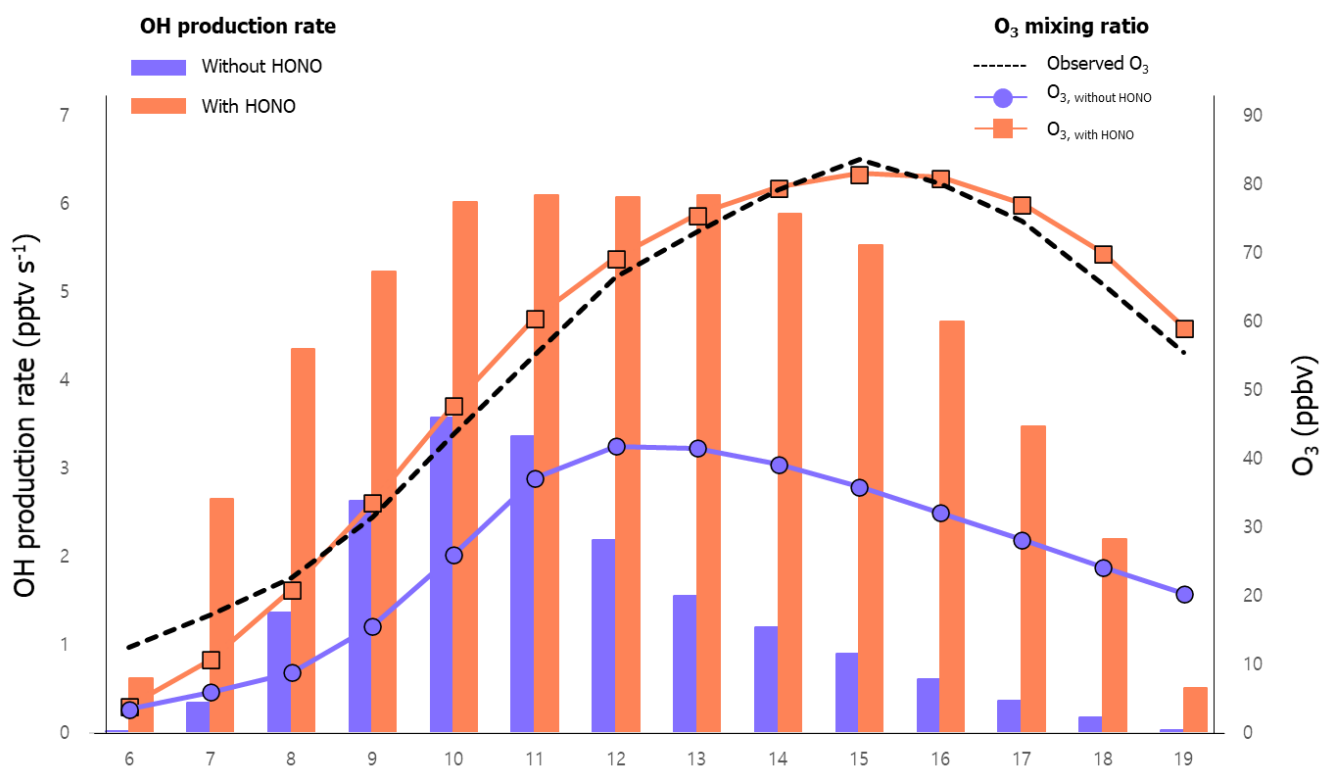
376

Figure 7. Relationship between measured HONO (HONO$_{obs}$) and modeled HONO (HONO$_{mod}$) using (a) RNDv1.0 and (b) a Random Forest model for the test dataset.

379

380

381

Figure 8. For June 2016, the diurnal variations of O_3 (line) and OH production rate (bar) calculated using the F0AM photochemical model with (orange) and without (blue) HONO estimated from the RNDv1.0 model. The measured and calculated O_3 values are compared.

385

386 **Table 1.** Resources for constructing the RND model.

	Version	Remark
Python	v3.8.3	
CUDA	v10.1	*If using GPU
CuDNN	v7.6.5	*If using GPU
Tensorflow	v2.3.0	*Python library*
Keras	v2.4.3	*Python library*
Pandas	v1.0.5	*Python library*
Numpy	v1.18.5	*Python library*

387 *GPU denotes graphic processing unit

388 **Table 2**. Input variables and their concentrations (10th–90th percentile of the hourly
389 measurements), coverage, and scale factors for the RNDv1.0 model. Measurements were
390 conducted in Seoul during May–June in 2016 and 2019.

	10th–90th percentile (unit)	Coverage (%)	Scale Factor1 (F_1)*	Scale Factor 2 (F_2)**
Input Variables				
O_3	12.1–90.4 (ppbv)	95.5	204.738	0.842
NO_2	11.0–48.6 (ppbv)	80.6	79.925	2.375
CO	252–743 (ppbv)	95.1	975.248	137.253
SO_2	1.9–6.4 (ppbv)	95.6	12.479	0.958
Solar Zenith Angle	22.7–118.4 (°)	100.0	112.317	14.195
Temperature	15.9–26.7 (°C)	99.4	24.240	8.610
Relative Humidity	29.2–79.1 (%)	99.4	88.545	10.555
Wind Speed	0.2–3.7 (m/s)	99.4	7.581	0.005
Wind Direction	45.4–287.5 (°)	99.4	359.565	0.235
Output Variables				
HONO	0.3–2.0 (ppbv)	81.1 %	3.447	0.013

391 * Maximum–Minimum
392 ** Minimum value

393

394 **Table 3.** Performance of the chemical transport model (CMAQv5.3.1) and machine learning
395 (ML) models, including Random Forest (RF), Artificial Neural Network (ANN), and RNDv1.0,
396 on the measurement data from 2016 KORUS-AQ campaign, which were used for training.

	CMAQv5.3.1	RF	ANN	RNDv1.0
IOA	0.44	0.99	0.86	0.9
r	−0.07	0.99	0.81	0.84
MAE	0.82	0.1	0.38	0.27
RMSE	1.06	0.12	0.41	0.37

397

398

399 **Table 4.** Results of the bootstrap test of measurement data used to train the RF and RNDv1.0

400 models. The greater the MAE, the greater the influence of the variable.

Variable	RF		RNDv1.0	
	MAE	Feature Importance	MAE	Feature Importance
-	0.10	-	0.28	-
O_3	0.57	1	0.29	8
NO_2	0.24	4	0.59	1
CO	0.19	7	0.37	5
SO_2	0.17	8	0.34	6
Solar zenith Angle (SZA)	0.25	2	0.41	4
Temperature (T)	0.21	5	0.52	2
Relative humidity (RH)	0.25	3	0.52	2
Wind speed (WS)	0.20	6	0.34	6
Wind direction (WD)	0.13	9	0.29	8

401

402

Reference

Akimoto, H., Nagashima, T., Li, J., Fu, J. S., Ji, D., Tan, J., and Wang, Z.: Comparison of surface ozone simulation among selected regional models in MICS-Asia III–effects of chemistry and vertical transport for the causes of difference, Atmospheric Chemistry and Physics, 19, 603-615, 2019.

Akimoto, H., and Tanimoto, H.: Review of Comprehensive Measurements of Speciated NOy and its Chemistry: Need for Quantifying the Role of Heterogeneous Processes of HNO3 and HONO, Aerosol and Air Quality Research, 21, 200395, 2021.

Anderson, D. C., Loughner, C. P., Diskin, G., Weinheimer, A., Canty, T. P., Salawitch, R. J., Worden, H. M., Fried, A., Mikoviny, T., and Wisthaler, A.: Measured and modeled CO and NOy in DISCOVER-AQ: An evaluation of emissions and chemistry over the eastern US, Atmospheric Environment, 96, 78-87, 2014.

Arcomano, T., Szunyogh, I., Wikner, A., Pathak, J., Hunt, B. R., and Ott, E.: A Hybrid Approach to Atmospheric Modeling that Combines Machine Learning with a Physics-Based Numerical Model, Journal of Advances in Modeling Earth Systems, e2021MS002712, 2021.

Armante, R., Perrin, A., Kwabia Tchana, F., and Manceron, L.: The v4 bands at 11 μm: linelists for the Trans-and Cis-conformer forms of nitrous acid (HONO) in the 2019 version of the GEISA database, Molecular Physics, e1951860, 2021.

Arnell, N. W., Lowe, J. A., Challinor, A. J., and Osborn, T. J.: Global and regional impacts of climate change at different levels of global temperature increase, Climatic Change, 155, 377-391, 2019.

Baek, W.-K., and Jung, H.-S.: Performance Comparison of Oil Spill and Ship Classification from X-Band Dual-and Single-Polarized SAR Image Using Support Vector Machine, Random Forest, and Deep Neural Network, Remote Sensing, 13, 3203, 2021.

Bao, F., Cheng, Y., Kuhn, U., Li, G., Wang, W., Kratz, A. M., Weber, J., Weber, B., Pöschl, U., and Su, H.: Key Role of Equilibrium HONO Concentration over Soil in Quantifying Soil–Atmosphere HONO Fluxes, Environmental science & technology, 2022.

Bengio, Y., and Grandvalet, Y.: No unbiased estimator of the variance of K-fold cross-validation, Citeseer, 2003.

Bloss, W. J., Kramer, L., Crilley, L. R., Vu, T., Harrison, R. M., Shi, Z., Lee, J. D., Squires, F. A., Whalley, L. K., and Slater, E.: Insights into air pollution chemistry and sulphate formation from nitrous acid (HONO) measurements during haze events in Beijing, Faraday Discussions, 226, 223-238, 2021.

Brown, S. S., An, H., Lee, M., Park, J.-H., Lee, S.-D., Fibiger, D. L., McDuffie, E. E., Dubé, W. P., Wagner, N. L., and Min, K.-E.: Cavity enhanced spectroscopy for measurement of nitrogen oxides in the Anthropocene: results from the Seoul tower during MAPS 2015, Faraday discussions, 200, 529-557, 2017.

Canty, T., Hembeck, L., Vinciguerra, T., Anderson, D., Goldberg, D., Carpenter, S., Allen, D., Loughner, C., Salawitch, R., and Dickerson, R.: Ozone and NO x chemistry in the eastern US: evaluation of CMAQ/CB05 with satellite (OMI) data, Atmospheric Chemistry and Physics, 15, 10965-10982, 2015.

Chen, G., Li, S., Knibbs, L. D., Hamm, N. A., Cao, W., Li, T., Guo, J., Ren, H., Abramson, M. J., and Guo, Y.: A machine learning method to estimate PM2. 5 concentrations across China with remote sensing, meteorological and land use information, Science of the Total Environment, 636, 52-60, 2018a.

Chen, Y., Wolke, R., Ran, L., Birmili, W., Spindler, G., Schröder, W., Su, H., Cheng, Y., Tegen, I., and Wiedensohler, A.: A parameterization of the heterogeneous hydrolysis of N2O5 for mass-based aerosol models: improvement of particulate nitrate prediction, Atmos. Chem. Phys, 18, 673-689, 2018b.

Cheng, P., Pour-Biazar, A., White, A. T., and McNider, R. T.: Improvement of summertime surface ozone prediction by assimilating Geostationary Operational Environmental Satellite cloud observations, Atmospheric Environment, 268, 118751, 2022.

Clarisse, L., R'Honi, Y., Coheur, P. F., Hurtmans, D., and Clerbaux, C.: Thermal infrared nadir observations of 24 atmospheric gases, Geophysical Research Letters, 38, 2011.

Cui, L., and Wang, S.: Mapping the daily nitrous acid (HONO) concentrations across China during 2006-2017 through ensemble machine-learning algorithm, Science of The Total Environment, 147325, 2021.

Dang, C., Liu, Y., Yue, H., Qian, J., and Zhu, R.: Autumn crop yield prediction using data-driven approaches:-support vector machines, random forest, and deep neural network methods, Canadian Journal of Remote Sensing, 47, 162-181, 2021.

Ding, B., Qian, H., and Zhou, J.: Activation functions and their characteristics in deep neural networks, 2018 Chinese control and decision conference (CCDC), 2018, 1836-1841.

Ge, B., Xu, X., Ma, Z., Pan, X., Wang, Z., Lin, W., Ouyang, B., Xu, D., Lee, J., and Zheng, M.: Role of Ammonia on the Feedback Between AWC and Inorganic Aerosol Formation During Heavy Pollution in the North China Plain, Earth and Space Science, 6, 1675-1693, 2019.

459 Gen, M., Liang, Z., Zhang, R., Mabato, B. R. G., and Chan, C. K.: Particulate nitrate photolysis in the atmosphere,
460 Environmental Science: Atmospheres, 2022.
461 Gil, J., Son, J., Kang, S., Park, J., Lee, M., Jeon, E., and Shim, M.: HONO measurement in Seoul during Summer
462 2018 and its Impact on Photochemistry, Journal of Korean Society for Atmospheric Environment, 36, 579-588,
463 10.5572/KOSAE.2020.36.5.579, 2020.
464 Gil, J.: RNDv1.0 and example, https://doi.org/10.5281/zenodo.5540180, in, Zenodo, 2021.
465 Gil, J., Kim, J., Lee, M., Lee, G., Ahn, J., Lee, D. S., Jung, J., Cho, S., Whitehill, A., Szykman, J., and Lee, J.:
466 Characteristics of HONO and its impact on O3 formation in the Seoul Metropolitan Area during the Korea-US Air
467 Quality study, Atmospheric Environment, 2021, https://doi.org/10.1016/j.atmosenv.2020.118182., 2021.
468 Gil, J.: Formation pathways of HONO and its impact on O3 and fine aerosol: based on measurement and modelling
469 study, Doctoral Thesis, 262, 2022.
470 Gu, R., Wang, W., Peng, X., Xia, M., Zhao, M., Zhang, Y., Liu, Y., Shen, H., Xue, L., and Wang, T.: Nitrous acid
471 in the polluted coastal atmosphere of the South China Sea: Ship emissions, budgets, and impacts, Science of The
472 Total Environment, 153692, 2022.
473 IPCC: Summary for policymakers. In:Climate Change 2014: Impacts, Adaption, and Vulnerability. Part A: Global
474 and Sectoral Aspects. Contribution of Working Group II to the Fifth Assessment Report of the Intergovernmental
475 Panel on Climate Change [Field, C.B., V.R. Barros, D.J. Dokken, K.J. Mach, M.D. Mastrandrea, T.E. Bilir, M.
476 Chatterjee, K.L. Ebi, Y.O. Estrada, R.C. Genova, B. Girma, E.S. Kissel, A.N. Levy, S. MacCracken, P.R.
477 Mastrandrea, and L.L.White (eds.)], Cambridge, United Kingdom and New York, NY, USA, 1-32, 2014.
478 Jia, C., Tong, S., Zhang, W., Zhang, X., Li, W., Wang, Z., Wang, L., Liu, Z., Hu, B., and Zhao, P.: Pollution
479 characteristics and potential sources of nitrous acid (HONO) in early autumn 2018 of Beijing, Science of The Total
480 Environment, 735, 139317, 2020.
481 Joutsensaari, J., Ozon, M., Nieminen, T., Mikkonen, S., Lähivaara, T., Decesari, S., Facchini, M. C., Laaksonen,
482 A., and Lehtinen, K. E.: Identification of new particle formation events with deep learning, Atmospheric Chemistry
483 and Physics, 18, 9597-9615, 2018.
484 Kang, Y., Choi, H., Im, J., Park, S., Shin, M., Song, C.-K., and Kim, S.: Estimation of surface-level NO2 and O3
485 concentrations using TROPOMI data and machine learning over East Asia, Environmental Pollution, 288, 117711,
486 2021.
487 Kim, H., Gil, J., Lee, M., Jung, J., Whitehill, A., Szykman, J., Lee, G., Kim, D., Cho, S., Ahn, J., Hong, J., and
488 Park, M.: Overview and characteristics of air quality in the Seoul Metropolitan Area during the KORUS-AQ
489 campaign, Elementa: Science of the Anthropocene, in review, 2020.
490 Kleffmann, J., Lörzer, J., Wiesen, P., Kern, C., Trick, S., Volkamer, R., Rodenas, M., and Wirtz, K.:
491 Intercomparison of the DOAS and LOPAP techniques for the detection of nitrous acid (HONO), Atmospheric
492 Environment, 40, 3640-3652, 2006.
493 Kleinert, F., Leufen, L. H., and Schultz, M. G.: IntelliO3-ts v1. 0: a neural network approach to predict near-surface
494 ozone concentrations in Germany, Geoscientific Model Development, 14, 1-25, 2021.
495 Krishnamurthy, R., Newsom, R. K., Berg, L. K., Xiao, H., Ma, P.-L., and Turner, D. D.: On the estimation of
496 boundary layer heights: a machine learning approach, Atmospheric Measurement Techniques, 14, 4403-4424,
497 2021.
498 Lee, B. H., Wood, E. C., Zahniser, M. S., McManus, J. B., Nelson, D. D., Herndon, S. C., Santoni, G., Wofsy, S.
499 C., and Munger, J. W.: Simultaneous measurements of atmospheric HONO and NO 2 via absorption spectroscopy
500 using tunable mid-infrared continuous-wave quantum cascade lasers, Applied Physics B, 102, 417-423, 2011.
501 Levy, M., Zhang, R., Zheng, J., Zhang, A. L., Xu, W., Gomez-Hernandez, M., Wang, Y., and Olaguer, E.:
502 Measurements of nitrous acid (HONO) using ion drift-chemical ionization mass spectrometry during the 2009
503 SHARP field campaign, Atmospheric Environment, 94, 231-240, 2014.
504 Li, S., Song, W., Zhan, H., Zhang, Y., Zhang, X., Li, W., Tong, S., Pei, C., Wang, Y., and Chen, Y.: Contribution of
505 Vehicle Emission and NO2 Surface Conversion to Nitrous Acid (HONO) in Urban Environments: Implications
506 from Tests in a Tunnel, Environmental Science & Technology, 55, 15616-15624, 2021a.
507 Li, Y., Wang, X., Wu, Z., Li, L., Wang, C., Li, H., Zhang, X., Zhang, Y., Li, J., and Gao, R.: Atmospheric nitrous
508 acid (HONO) in an alternate process of haze pollution and ozone pollution in urban Beijing in summertime:
509 Variations, sources and contribution to atmospheric photochemistry, Atmospheric Research, 260, 105689, 2021b.
510 Li, Z., Xie, P., Hu, R., Wang, D., Jin, H., Chen, H., Lin, C., and Liu, W.: Observations of N2O5 and NO3 at a
511 suburban environment in Yangtze river delta in China: Estimating heterogeneous N2O5 uptake coefficients,
512 Journal of Environmental Sciences, 2020.
513 Liebmann, J., Karu, E., Sobanski, N., Schuladen, J., Ehn, M., Schallhart, S., Quéléver, L., Hellen, H., Hakola, H.,
514 and Hoffmann, T.: Direct measurement of NO3 radical reactivity in a boreal forest, Atmospheric Chemistry and
515 Physics, 2018.

Liu, Y., Lu, K., Li, X., Dong, H., Tan, Z., Wang, H., Zou, Q., Wu, Y., Zeng, L., and Hu, M.: A comprehensive model test of the HONO sources constrained to field measurements at rural North China Plain, Environmental science & technology, 53, 3517-3525, 2019.

Mallet, V., and Sportisse, B.: Uncertainty in a chemistry-transport model due to physical parameterizations and numerical approximations: An ensemble approach applied to ozone modeling, Journal of Geophysical Research: Atmospheres, 111, 2006.

Meng, F., Qin, M., Fang, W., Duan, J., Tang, K., Zhang, H., Shao, D., Liao, Z., Feng, Y., and Huang, Y.: Measurement of HONO flux using the aerodynamic gradient method over an agricultural field in the Huaihe River Basin, China, Journal of Environmental Sciences, 2022.

Monks, P. S., Archibald, A., Colette, A., Cooper, O., Coyle, M., Derwent, R., Fowler, D., Granier, C., Law, K. S., and Mills, G.: Tropospheric ozone and its precursors from the urban to the global scale from air quality to short-lived climate forcer, Atmospheric Chemistry and Physics, 15, 8889-8973, 2015.

Myhre, G., Aas, W., Cherian, R., Collins, W., Faluvegi, G., Flanner, M., Forster, P., Hodnebrog, Ø., Klimont, Z., and Lund, M. T.: Multi-model simulations of aerosol and ozone radiative forcing due to anthropogenic emission changes during the period 1990–2015, Atmospheric Chemistry and Physics, 17, 2709-2720, 2017.

Pinto, J., Dibb, J., Lee, B., Rappenglück, B., Wood, E., Levy, M., Zhang, R. Y., Lefer, B., Ren, X. R., and Stutz, J.: Intercomparison of field measurements of nitrous acid (HONO) during the SHARP campaign, Journal of Geophysical Research: Atmospheres, 119, 5583-5601, 2014.

Reichstein, M., Camps-Valls, G., Stevens, B., Jung, M., Denzler, J., and Carvalhais, N.: Deep learning and process understanding for data-driven Earth system science, Nature, 566, 195-204, 2019.

Roberts, J. M., Veres, P., Warneke, C., Neuman, J., Washenfelder, R., Brown, S., Baasandorj, M., Burkholder, J., Burling, I., and Johnson, T. J.: Measurement of HONO, HNCO, and other inorganic acids by negative-ion proton-transfer chemical-ionization mass spectrometry (NI-PT-CIMS): Application to biomass burning emissions, Atmospheric Measurement Techniques, 3, 981, 2010.

Schultz, M., Betancourt, C., Gong, B., Kleinert, F., Langguth, M., Leufen, L., Mozaffari, A., and Stadtler, S.: Can deep learning beat numerical weather prediction?, Philosophical Transactions of the Royal Society A, 379, 20200097, 2021.

Shahriar, S. A., Kayes, I., Hasan, K., Salam, M. A., and Chowdhury, S.: Applicability of machine learning in modeling of atmospheric particle pollution in Bangladesh, Air Quality, Atmosphere & Health, 13, 1247-1256, 2020.

Shareef, M. M., Husain, T., and Alharbi, B.: Studying the Effect of Different Gas-Phase Chemical Kinetic Mechanisms on the Formation of Oxidants, Nitrogen Compounds and Ozone in Arid Regions, Journal of Environmental Protection, 10, 1006-1031, 2019.

Shindell, D. T., Lamarque, J.-F., Schulz, M., Flanner, M., Jiao, C., Chin, M., Young, P., Lee, Y. H., Rotstayn, L., and Mahowald, N.: Radiative forcing in the ACCMIP historical and future climate simulations, Atmospheric Chemistry and Physics, 13, 2939-2974, 2013.

Stadtler, S., Simpson, D., Schröder, S., Taraborrelli, D., Bott, A., and Schultz, M.: Ozone impacts of gas–aerosol uptake in global chemistry transport models, Atmospheric chemistry and physics, 18, 3147-3171, 2018.

Stevenson, D., Young, P., Naik, V., Lamarque, J.-F., Shindell, D. T., Voulgarakis, A., Skeie, R. B., Dalsoren, S. B., Myhre, G., and Berntsen, T. K.: Tropospheric ozone changes, radiative forcing and attribution to emissions in the Atmospheric Chemistry and Climate Model Intercomparison Project (ACCMIP), Atmospheric Chemistry and Physics, 13, 3063-3085, 2013.

Sumathi, S., and Pugalendhi, G. K.: Cognition based spam mail text analysis using combined approach of deep neural network classifier and random forest, Journal of Ambient Intelligence and Humanized Computing, 12, 5721-5731, 2021.

Sun, Y., Wang, L., Wang, Y., Quan, L., and Zirui, L.: In situ measurements of SO2, NOx, NOy, and O3 in Beijing, China during August 2008, Science of the Total Environment, 409, 933-940, 2011.

Theys, N., Volkamer, R., Müller, J.-F., Zarzana, K. J., Kille, N., Clarisse, L., De Smedt, I., Lerot, C., Finkenzeller, H., and Hendrick, F.: Global nitrous acid emissions and levels of regional oxidants enhanced by wildfires, Nature geoscience, 13, 681-686, 2020.

Tie, X., Geng, F., Guenther, A., Cao, J., Greenberg, J., Zhang, R., Apel, E., Li, G., Weinheimer, A., and Chen, J.: Megacity impacts on regional ozone formation: observations and WRF-Chem modeling for the MIRAGE-Shanghai field campaign, Atmospheric Chemistry and Physics, 13, 5655-5669, 2013.

VandenBoer, T., Markovic, M., Sanders, J., Ren, X., Pusede, S., Browne, E., Cohen, R., Zhang, L., Thomas, J., and Brune, W. H.: Evidence for a nitrous acid (HONO) reservoir at the ground surface in Bakersfield, CA, during CalNex 2010, Journal of Geophysical Research: Atmospheres, 119, 9093-9106, 2014.

Varotsos, K., Giannakopoulos, C., and Tombrou, M.: Assessment of the Impacts of climate change on european ozone levels, Water, Air, & Soil Pollution, 224, 1-13, 2013.

573 Wang, H., Chen, X., Lu, K., Hu, R., Li, Z., Wang, H., Ma, X., Yang, X., Chen, S., and Dong, H.: NO3 and N2O5
574 chemistry at a suburban site during the EXPLORE-YRD campaign in 2018, Atmospheric Environment, 224,
575 117180, 2020.
576 Wang, T., Qin, Z., and Zhu, M.: An ELU network with total variation for image denoising, International Conference
577 on Neural Information Processing, 2017a, 227-237.
578 Wang, X., Wang, H., Xue, L., Wang, T., Wang, L., Gu, R., Wang, W., Tham, Y. J., Wang, Z., and Yang, L.:
579 Observations of N2O5 and ClNO2 at a polluted urban surface site in North China: High N2O5 uptake coefficients
580 and low ClNO2 product yields, Atmospheric environment, 156, 125-134, 2017b.
581 Wolfe, G. M., Marvin, M. R., Roberts, S. J., Travis, K. R., and Liao, J.: The framework for 0-D atmospheric
582 modeling (F0AM) v3. 1, Geoscientific Model Development, 9, 3309, 2016.
583 Xu, Z., Liu, Y., Nie, W., Sun, P., Chi, X., and Ding, A.: Evaluating the measurement interference of wet rotating-
584 denuder–ion chromatography in measuring atmospheric HONO in a highly polluted area, Atmospheric
585 Measurement Techniques, 12, 6737-6748, 2019.
586 Xue, C., Ye, C., Ma, Z., Liu, P., Zhang, Y., Zhang, C., Tang, K., Zhang, W., Zhao, X., and Wang, Y.: Development
587 of stripping coil-ion chromatograph method and intercomparison with CEAS and LOPAP to measure atmospheric
588 HONO, Science of The Total Environment, 646, 187-195, 2019.
589 Ye, C., Zhou, X., Pu, D., Stutz, J., Festa, J., Spolaor, M., Tsai, C., Cantrell, C., Mauldin, R. L., and Campos, T.:
590 Rapid cycling of reactive nitrogen in the marine boundary layer, Nature, 532, 489-491, 2016.
591